Effect of insoluble surfactants on a thermocapillary flow

Franco N. Piñan Basualdo,[1, 2, a)] R. Terrazas Mallea,[3] B. Scheid,[1] A. Bolopion,[2] M. Gauthier,[2] and P. Lambert[1]

[1)]*Transfers, Interfaces and Processes (TIPs), Ecole Polytechnique de Bruxelles (CP 165/67), Université Libre de Bruxelles, Avenue Franklin Roosevelt 50, 1050 Brussels, Belgium.*

[2)]*FEMTO-ST Institute, Université Bourgogne Franche-Comté/CNRS, 24 rue Savary, F-25000 Besançon, France.*

[3)]*Institute of Physical Chemistry, Polish Academy of Sciences, Kasprzaka 44/52,01-224 Warsaw, Poland.*

(Dated: 29 September 2021)

The thermocapillary effect, arising flow due to a temperature gradient along a fluid interface, is the dominant effect in some industrial and microfluidics processes and must be studied in order to optimise them. In this work, we analyse how insoluble surfactants adsorbed at the interface can affect such a flow. In particular, we analyse the case where the thermocapillary flow is induced at the air-water interface by locally heating it with an infrared laser, setup that is used to manipulate floating particles through the generated flow. Since water is a polar fluid, the air-water interface is easily polluted by surfactants. We developed a numerical model considering the uncontrolled presence of surfactants, which evidences that the effect of the surface contamination cannot be neglected, even for small surfactants concentration. The results of this numerical model were compared with different experimental measurements: particle tracking velocimetry, convection cell radius measurements and thermography of the surface. All the experimental observations agree with the numerical model with the initial surface contamination being a fitting parameter. The model was then validated comparing its results with measurements for which a known quantity of surfactant was added to the interface. Finally, an analytical model was developed to explain the effects of the governing parameters, which agrees with the simulations and the experimental results. The developed models give us insights towards the miniaturization of the manipulation platform.

I. INTRODUCTION

Whenever a gradient of temperature exists along a fluid interface, an interfacial flow will arise due to the resulting surface stress[1]. This effect, known as thermocapillary effect, has a strong impact in industrial processes, like welding[2] and solidification[3]. More recently, several applications have been developed in the field of microfluidics: a thermocapillary pump[4], droplets generation[5] and migration[6,7], bubbles migration[8,9], and particles manipulation[10]. These applications require understanding and controlling the thermocapillary flow. Experimentally, it can be difficult to obtain a perfectly clean fluid interface. Adsorbed impurities act like surfactants that rigidify the interface[11,12], effect known as surface elasticity, and can affect the thermocapillary flow. The presence of such an adsorbed layer of surfactants has been observed to cause symmetry breaking instabilities[13,14] under some conditions. The stable regime has also been studied[15] in a thin water layer, under 2D configuration. Therefore, in this manuscript we close the gap and study the effect of an adsorbed layer of surfactants on the symmetric thermocapillary flow in a cylindrical configuration and a thick water layer.

In particular, we analyse the case where an infrared (IR) laser is used to generate a localized temperature increase at an air-water interface, inducing a thermocapillary flow. Such a configuration has been previously used to manipulate particles at the air-water interface[16,17]. Water was selected as a fluid due to its high surface tension and low viscosity, giving place to high fluid velocities

---

a)Electronic mail: Franco.Pinan.Basualdo@ulb.be

($\approx 30\,\mathrm{mm/s}$). However, since water is a polar fluid, impurities can easily be trapped at the interface, which makes almost impossible to have a completely pure air-water interface. In Section II, we first introduced the theoretical frame and our particular problem. Then in Section III, we present the developed numerical model and compare its results and with three experimental measurements: Particle tracking velocimetry, convection cell radius and thermography measurements. Finally, in Section IV we present the developed analytical model and compare its predictions with the simulation's and experiments' results. We find that no matter how small the amount of impurities is, the induced surface elasticity always has an effect on the flow, similarly to how a low fluid viscosity can completely change the flow profile compared to the inviscid case. The developed models help us to better understand the flow generation and give us insights towards the miniaturization of the thermocapillary manipulation platform.

II. PHYSICAL CONSIDERATIONS

In this section, we first introduce the theoretical frame of the work. Then, we present the particular problem we focus on, and we introduce the non-dimensional parameters governing the system.

A. Theoretical frame

Surface tension (σ) can be defined as the required energy to increase the area of an interface per unit area ($\sigma = \partial E/\partial A$). It is known that surface tension depends on the temperature and on the concentration of some species[18]. In particular, some big molecules, known as surfactants, that have a hydrophobic tail and a hydrophilic head, adsorb at air-water or oil-water interfaces. They adsorb with their heads in the water phase and their tails in the other one, and reduce the surface tension[19]. When a gradient of surface tension exists along the interface, whether it is due to a temperature or concentration gradient, a surface stress arises ($\tau_\sigma = \nabla_S \sigma$). This stress is balanced by the viscous shear stress of each phase, resulting in

$$\mu_1 \frac{\partial \mathbf{U_1}}{\partial \mathbf{n}} - \mu_2 \frac{\partial \mathbf{U_2}}{\partial \mathbf{n}} = \nabla_S \sigma \tag{1}$$

where $\mathbf{U_i}$ and μ_i are the velocity vector and the dynamic viscosity of the fluid i respectively, and $\mathbf{n}$ is the interface normal vector pointing from phase 1 to phase 2. The operator ∇_S is the surface gradient operator ($\nabla_S \sigma = \nabla \sigma - \mathbf{n}(\mathbf{n} \cdot \nabla \sigma)$). In case of a liquid-gas interface, the gas' phase viscous stress can be neglected in (1). If we also assume that there is only one species of surfactant, we can write

$$\mu \frac{\partial \mathbf{U}}{\partial \mathbf{n}} = -(\gamma_T \nabla_S T + \gamma_\Gamma \nabla_S \Gamma) \tag{2}$$

where T is the temperature, Γ is the surface surfactant concentration, $\gamma_T = -\partial \sigma/\partial T$ and $\gamma_\Gamma = -\partial \sigma/\partial \Gamma$ are positive values hereby assumed constant. This last approximation is valid for low surfactant concentrations (for higher concentrations $\partial \sigma/\partial \Gamma = -E_S/\Gamma$ where E_S if the surface elasticity[12]). It can be seen that, through (2), the momentum equation gets coupled with the energy and the surfactant transport equations at the interface. The surfactant transport equation can be complex for soluble surfactants, due to adsorption dynamics, or deformable interfaces[20], but in the case of an insoluble surfactant and a non-deformable interface, this equation is reduced to

$$\frac{\partial \Gamma}{\partial t} + \nabla_S \cdot (\mathbf{U}\Gamma) = D_S \nabla_S^2 \Gamma, \tag{3}$$

where D_S is a surface diffusion coefficient.

B. Particular problem

In our case[16,17], we study the geometry shown in Fig. 1. A cylindrical volume of water whose top surface, in contact with air and where a layer of insoluble surfactants is adsorbed, is heated from above by an infrared laser beam pointed at the centre of the water-air interface. Qualitatively, once the laser is turned on, the temperature at the centre increases, creating a positive radial surface tension gradient, giving place to a positive radial flow. Because of mass conservation, a negative radial flow arises deep below the surface, generating a toroidal convection cell as shown by the arrows in Fig. 2a (Multimedia view). The radial flow at the free surface generates a depletion of surfactants around the laser spot, increasing the surface tension and counteracting the effect of the temperature increase.

Besides the insolubility of the surfactants, we make further assumptions to simplify the modelling: the interface deformations, the heat transfer to the air phase, and the buoyancy forces are neglected.

Indeed, surface deformations are considerable only for thin fluid layers[21,22]. The vertical deformation of the interface in a similar configuration[23] has been predicted to be $\Delta H/R_L = \gamma_T \Delta T/\sigma_0$. If we consider $\Delta T \approx 2\,\mathrm{K}$ (the measured temperature increase for a laser power $P_L = 40\,\mathrm{mW}$), we obtain $\Delta H/R_L \approx 0.004$, thus validating our assumption.

On the other hand, the heat transfer towards the air phase can be compared to the heat conduction in the water phase through the Biot number $Bi = hR_L/\kappa$, where h is the heat transfer coefficient to the air phase. Typical values for free convection of air[24] are $h < 25\,\mathrm{W/m^2\,K}$, thus obtaining $Bi < 0.03$ and validating our assumption.

Finally, the strength of buoyancy forces can be compared to thermocapillary forces through the dynamic Bond number $Bo_d = \rho\beta g R_L^2/\gamma_T = 0.005$, where $\beta = 200 \times 10^{-6}\,\mathrm{K^{-1}}$ is the thermal expansion coefficient of water, and $g = 9.8\,\mathrm{m/s^2}$ is the gravitational acceleration.

In order to explain the absorption of the energy provided by the laser, we consider the light attenuation coefficient of water $\alpha = 3280\,\mathrm{m^{-1}}$ defined for the used wavelength ($\lambda = 1455\,\mathrm{nm}$). Assuming a collimated Gaussian beam with a waist radius R_L, the absorbed volumetric power $\dot{q}_L$ (energy per unit volume and unit time) is[23]

$$\dot{q}_L = \frac{2P_L\alpha}{\pi R_L^2} \exp\left(-2\left(\frac{r}{R_L}\right)^2 - \alpha z\right) \tag{4}$$

where P_L is the laser power, r the radial coordinate, and z the vertical coordinate, with origin at the interface. Finally, (3) and (4) together with the mass, momentum (Navier-Stokes), and energy conservation complete the set of equations. Zero velocity, homogeneous temperature ($T = T_0$) and homogeneous surfactant concentration ($\Gamma = \Gamma_0$) are used as initial conditions. Regarding boundary conditions, we considered no slip, thermal insulation and zero surfactant flux boundary conditions on the lateral recipient walls, no slip and constant temperature on the bottom wall, and zero vertical velocity, (2), and thermal insulation at the air-water interface. For the detailed set of equations in cylindrical coordinates under the assumption of a flat interface, see the Supplementary Material.

These equations can be made non-dimensional by using R_L as the characteristic length, $\tilde{t} = t\mu/\rho R_L^2$ as the non-dimensional time, $\tilde{\mathbf{U}} = \mathbf{U}\rho R_L/\mu$ as the non-dimensional velocity, $\tilde{P} = P\rho R_L^2/\mu^2$ as the non-dimensional pressure, $\Theta = (T - T_0)\kappa R_L/P_L$ as the non-dimensional temperature, and $\tilde{\Gamma} = \Gamma/\Gamma_0$ as the non-dimensional surfactant concentration. The resulting set of equations is

$$\tilde{\nabla} \cdot \tilde{\mathbf{U}} = 0 \tag{5}$$

$$\frac{\partial \tilde{\mathbf{U}}}{\partial \tilde{t}} + \tilde{\mathbf{U}} \cdot \tilde{\nabla}\tilde{\mathbf{U}} = -\tilde{\nabla}\tilde{P} + \tilde{\nabla}^2\tilde{\mathbf{U}} \tag{6}$$

$$\frac{\partial \Theta}{\partial \tilde{t}} + \tilde{\mathbf{U}} \cdot \tilde{\nabla}\Theta = \frac{1}{Pr}\left(\tilde{\nabla}^2\Theta + \mathring{q}_L\right) \tag{7}$$

where $\mathring{q}_L = 2\psi\exp\left(-2\tilde{r}^2 - \psi\tilde{z}\right)/\pi$ is the dimensionless absorbed volumetric power, $\psi = \alpha R_L$ describes the aspect ratio of the heated volume, and $Pr = \mu c_p/\kappa$ is the Prandtl number. At the inter-

TABLE I: Parameters' values used in this work.

Density	ρ	$997\,\text{kg/m}^3$
Dynamic viscosity	μ	$1.002\,\text{mPa s}$
Thermal conductivity	κ	$0.607\,\text{W/m K}$
Specific heat capacity	c_p	$4181\,\text{J/kg K}$
Surface tension ($T = 20\,°C$)	σ_0	$72.9\,\text{mN/m}$
Thermocapillary coeff.	γ_T	$155\,\mu\text{N/m K}$
Laser wavelength	λ	$1455\,\text{nm}$
Light attenuation coeff.	α	$3280\,\text{m}^{-1}$
Laser waist radius	R_L	$630\,\mu\text{m}$
Recipient radius	R_r	$25\,\text{mm}$
Recipient height	H_r	$7.5\,\text{mm}$
Laser power	P_L	$20\,\text{mW}$ to $200\,\text{mW}$
Surfactant surface pressure	$\gamma_\Gamma \Gamma_0$	$0\,\mu\text{N/m}$ to $150\,\mu\text{N/m}$
Surfactant diffusion coeff.	D_S	$1 \times 10^{-7}\,\text{m}^2/\text{s}$

TABLE II: Governing non-dimensional parameters and the values used in this work.

Heated volume aspect ratio	$\psi = \alpha R_L$	2
Prandtl number	$Pr = \mu c_p / \kappa$	7
Schmidt number	$Sc = \mu / \rho D_S$	10
Thermocapillary number	$C_T = \rho \gamma_T P_L / \mu^2 \kappa$	5×10^3 to 5×10^4
Solutocapillary number	$C_S = \rho \gamma_\Gamma \Gamma_0 R_L / \mu^2$	20 to 80

face, (3) and (2) result

$$\frac{\partial \tilde{\Gamma}}{\partial \tilde{t}} + \tilde{\nabla}_S \cdot (\tilde{\mathbf{U}} C) = \frac{1}{Sc} \tilde{\nabla}_S^2 \tilde{\Gamma} \tag{8}$$

$$\frac{\partial \tilde{\mathbf{U}}}{\partial \tilde{\mathbf{n}}} = -\left(C_T \tilde{\nabla}_S \Theta + C_S \tilde{\nabla}_S \tilde{\Gamma} \right) \tag{9}$$

where $Sc = \mu / \rho D_S$ is the surface Schmidt number, $C_T = \rho \gamma_T P_L / \mu^2 \kappa$ is the thermocapillary number, and $C_S = \rho \gamma_\Gamma \Gamma_0 R_L / \mu^2$ is the solutocapillary number. For the numerical values of these non-dimensional parameters, see Table II. For the detailed set of non-dimensional equations in cylindrical coordinates under the assumption of a flat interface, see the Supplementary Material.

III. RESULTS

In this section, we first present our numerical model and its results, observing three different regimes. Secondly, we compare the simulation results with three different experimental measurements (with an uncontrolled initial surfactant surface pressure): particle tracking velocimetry (PTV), convection cell radius and thermography measurements. Finally, a controlled quantity of surfactants was added to the interface and the thermography measurements was repeated, validating our numerical model without any fitting parameter.

A. Simulation results

Finite elements, axisymmetric, time dependent simulations were performed using Comsol multiphysics with the parameters shown in Table II, $\tilde{H}_r = 10$, and $\tilde{R}_r = 40$. For more details on the geometry discretization, see Supplementary Material. The results have been observed to be independent on the recipient height $\tilde{H}_r$ and its radius $\tilde{R}_r$ provided they are larger than a minimum threshold value ($\tilde{H}_r > 7.5$, $\tilde{R}_r > 30$ respectively) for the standard case ($C_T = 1 \times 10^4$ and $C_S = 30$).

Depending on the values of C_S and C_T, three regimes were observed: the convective, the transition and the conductive regime.
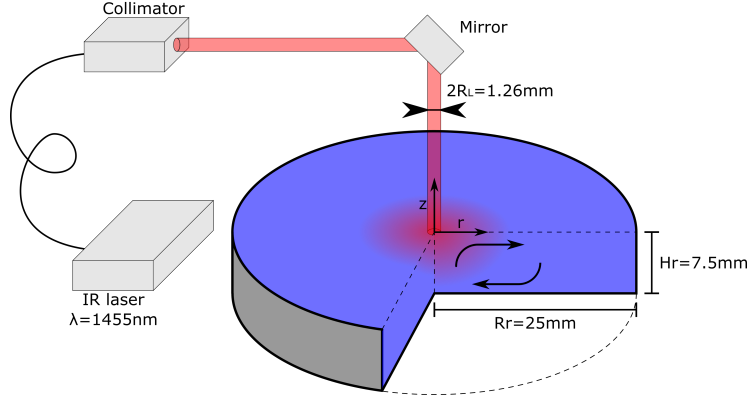
FIG. 1: Schematics of the system. An infrared laser (Keopsys Fiber Raman Laser CRFL-01-1455-OM1-B130-FA, wavelength $\lambda = 1455$ nm, output power of up to 1 W) is collimated and used to heat the air-water interface of a cylindrical volume of water (radius $R_r = 25$ mm and height $H_r = 7.5$ mm) from above. The laser waist diameter is $2R_L = 1.26$ mm (at the interface) and it is assumed to be constant (collimated beam).
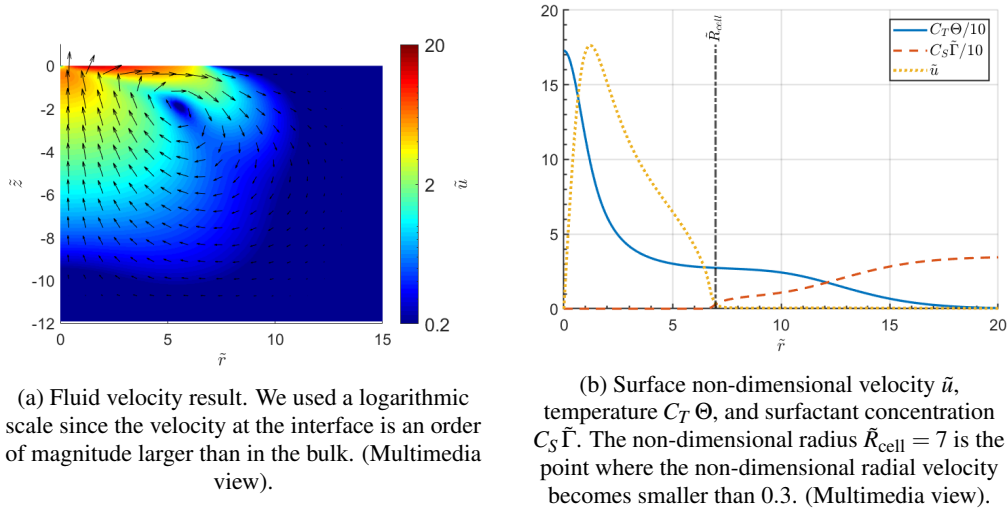

(a) Fluid velocity result. We used a logarithmic scale since the velocity at the interface is an order of magnitude larger than in the bulk. (Multimedia view).

(b) Surface non-dimensional velocity $\tilde{u}$, temperature $C_T \Theta$, and surfactant concentration $C_S \tilde{\Gamma}$. The non-dimensional radius $\tilde{R}_{\text{cell}} = 7$ is the point where the non-dimensional radial velocity becomes smaller than 0.3. (Multimedia view).

FIG. 2: Simulation results in the convective regime for $C_T = 1 \times 10^4$, and $C_S = 30$. The results correspond to $\tilde{t} = 25$.

If C_S is small enough and C_T large enough, we observe the convective regime. In this regime, a central area with no surfactant and a positive radial flow is obtained as shown in Fig. 2 (Multimedia view). Beyond a given radius, the surface tension gradients induced by temperature and concentration cancel each other and, according to (9), the shear stress at the surface vanishes. This radius coincides with R_{cell}, the radius at which the surface radial velocity vanishes, (see the non-dimensional $\tilde{R}_{\text{cell}} = R_{\text{cell}}/R_L$ in Fig. 2b). In addition, in this regime the maximum fluid velocity and temperature increase have been found to be independent of C_S. This is the regime we observe experimentally without added surfactant.

The transition regime is obtained for intermediate values of C_S and C_T. In this regime, $\tilde{R}_{\text{cell}}$ approaches unity and the maximum fluid velocity and temperature were found to depend on C_S (the first one decreases and the second one increases with C_S).

Finally, for large enough values of C_S and small enough values of C_T, we obtain the conductive regime. In this regime, the effect of the temperature is not strong enough to create a complete
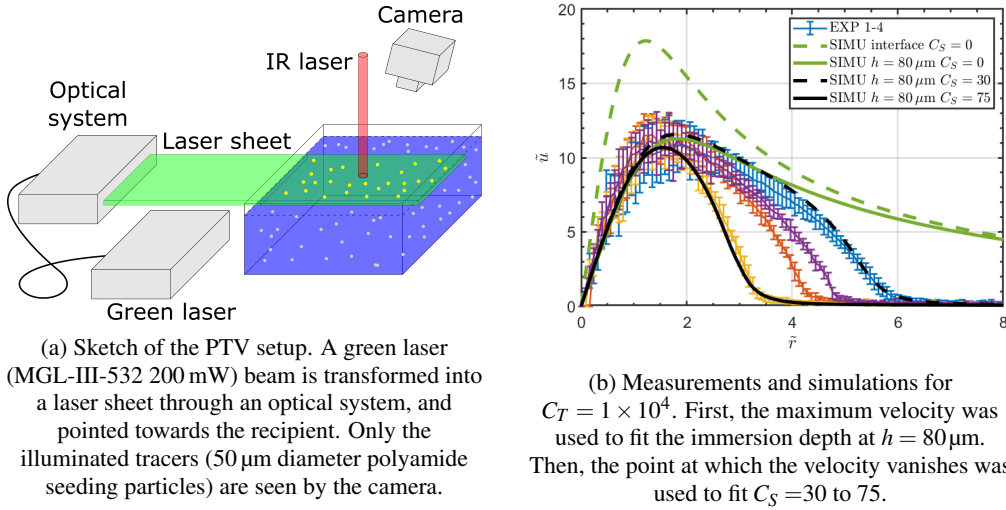
(a) Sketch of the PTV setup. A green laser (MGL-III-532 200 mW) beam is transformed into a laser sheet through an optical system, and pointed towards the recipient. Only the illuminated tracers (50 μm diameter polyamide seeding particles) are seen by the camera.

(b) Measurements and simulations for $C_T = 1 \times 10^4$. First, the maximum velocity was used to fit the immersion depth at $h = 80\,\mu$m. Then, the point at which the velocity vanishes was used to fit $C_S = 30$ to 75.

FIG. 3: PTV measurement setup and comparison between measurements and simulations.

depletion of surfactants at the laser spot. The stable state is a zero fluid velocity in the whole domain, since the surfactants completely counteract the temperature gradient. Therefore, the temperature profile is governed by heat conduction alone. We can find the limiting value for this regime as the point where the maximum temperature surface pressure is equal to the surfactant surface pressure: $C_{S\lim} = C_T \Theta_c$ where Θ_c is the value of Θ at the centre of the interface for a conduction only case. By performing a conduction only simulation to estimate Θ_c, we find $C_{S\lim} \approx 0.2 C_T$.

B.   Experimental results

The experimental validation of the above described numerical results was performed through three experimental observations (with an unknown surface contamination): particle tracking velocimetry (PTV), convection cell radius and thermography measurements. All this measurements were performed in the convective regime. The PTV measurement allowed us observe the effect of contamination, but it could not be performed exactly at the interface. The convection cell radius measurement could be performed at the interface, but it does not allow us to observe the radial distribution. Finally, the thermography measurement allowed us to obtain the temperature distribution at the interface. Then, a controlled quantity of surfactant was added to the interface and the thermography measurements was repeated to validate our numerical model without any fitting parameter. However, with the added surfactant, the system was in the transient regime.

1.   PTV measurements

To measure the flow velocity close to the air/water interface, the particle tracking velocimetry (PTV) method[25,26] was used. A sketch of the setup is shown in Fig. 3a. The optical system is composed of a green laser (MGL-III-532 200 mW) which is coupled to a fiber (Thorlabs P5-460B-PCAPC-1). Following the design methodology presented in Ref. 27, a set of convex and concave lenses was used to generate a thin collimated laser sheet, which was then used to illuminate the air-water interface. Polyamide seeding particles with a diameter of 50 μm (Dantec Dynamics PSP-50) were submerged in the water bulk and stirred before each measurement. Because the seeding particles were only slightly denser than water ($\rho = 1030\,\text{kg/m}^3$) the convective flow was strong enough to move them along. The laser sheet was placed so that it would be as close as possible to the interface but ensuring that enough particles could be detected by the camera to reconstruct the flow velocity around the laser spot using the software presented in Ref. 28. As the exact
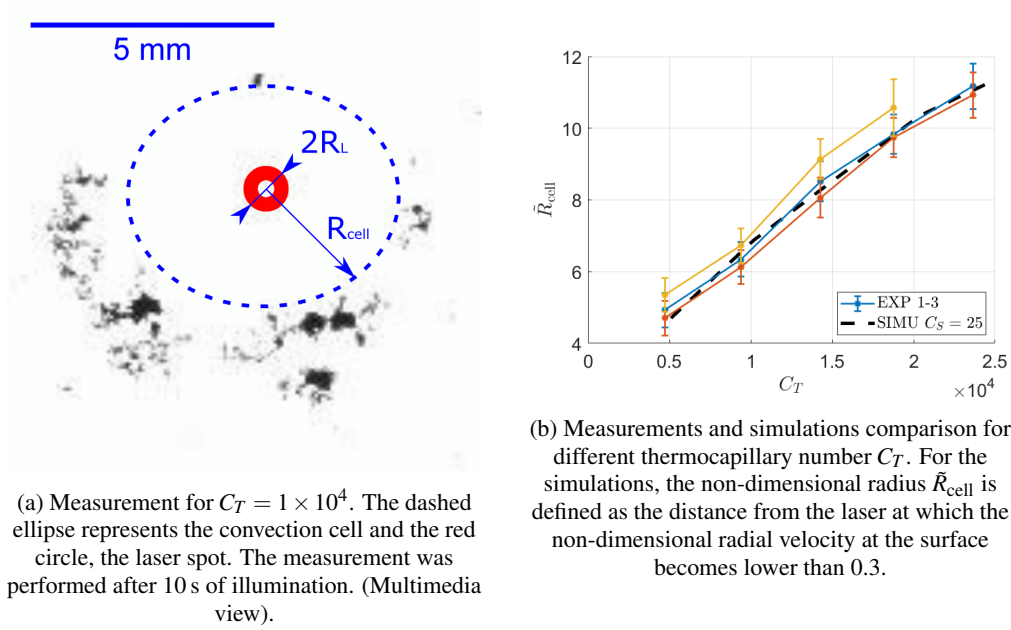
(a) Measurement for $C_T = 1 \times 10^4$. The dashed ellipse represents the convection cell and the red circle, the laser spot. The measurement was performed after 10 s of illumination. (Multimedia view).

(b) Measurements and simulations comparison for different thermocapillary number C_T. For the simulations, the non-dimensional radius $\tilde{R}_{\text{cell}}$ is defined as the distance from the laser at which the non-dimensional radial velocity at the surface becomes lower than 0.3.

FIG. 4: Convection cell superficial radius measurement and comparison with simulations

experimental immersion depth of the laser sheet is unknown and due to its strong influence on the fluid velocity, it was decided to turn it into a fitting parameter. The immersion depth mainly affects the maximum value for the radial velocity while C_S mainly affects the point at which the velocity becomes zero. First an immersion depth of 80 μm (comparable with the size of the particles) was fitted using the maximum velocity value. Then, C_S was fitted between 30 and 75 to rationalize the measurements. The process is shown in Fig. 3b. The variation between each experimental measurement can be explained by a different initial surfactant concentration in each water sample. Our model considering an initial surface contamination succeeds in predicting a limited range of the laser effect, in contrast with the model that did not consider the surface contamination. Moreover, our model can explain the difference between measurements as the result of different contamination levels among different water samples.

2. Convection cell radius at the surface

To eliminate the immersion depth dependence, we decided to look directly at the interface. Some aluminium flakes (typical size 71 μm) were deposited on the water surface, where they float thanks to the surface tension[29]. They are used as tracers to observe the surface flow since their inertia is low (Stokes number $St < 0.3$). Then, the laser was pointed towards a cluster of these floating flakes for at least 10 s, where the generated thermocapillary flow repelled the flakes from the laser. The mean radius R_{cell} of the area without flakes was estimated using the area entrapped by the dashed line shown in Fig. 4a (Multimedia view) where the central circle represents the laser spot. For the simulations results, since the surface velocity never becomes exactly zero, the non-dimensional radius $\tilde{R}_{\text{cell}}$ was defined as the point at which the non-dimensional radial velocity at the surface $\tilde{u}$ becomes lower than 0.3. The obtained $\tilde{R}_{\text{cell}}$ value is not very sensitive to the threshold value in the range 0.3 to 1, but quickly increases for lower values (for more details, see Supplementary Material). The comparison between experimental measurements and simulations can be seen in Fig. 4b where the measurements agree with the results obtained with a fitting parameter $C_S = 25$ (which is comparable to the lower value used to fit the PTV measurement $C_S = 30$). In this case, we did not observe a considerable variation among different water samples.
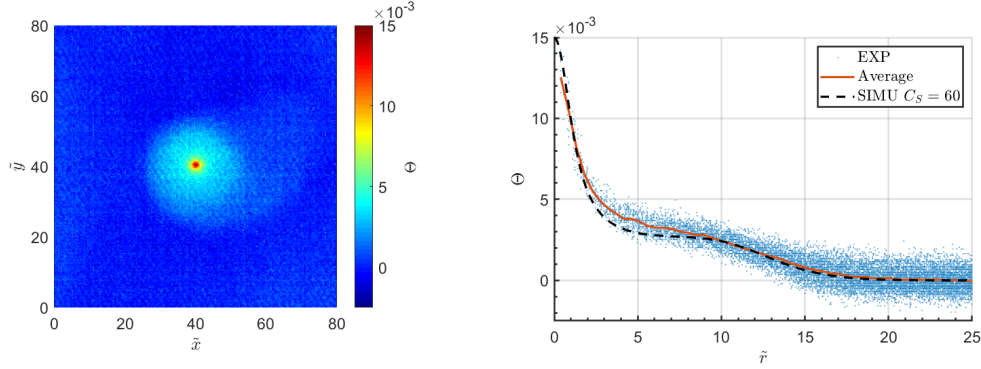
(a) Difference between a first image taken before turning the laser on, and a second one 30 s after. A constant value was added ($< 0.5\,\mathrm{K}$) to compensate the deviations and make the temperature increase far from the laser vanish.

(b) Comparison with simulations. The distance to the centre and the temperature was computed for each pixel. The results were compared with the simulations, fitting $C_S = 60$.

FIG. 5: Thermography results and comparison with simulations for $C_T = 2 \times 10^4$

3. Thermography of the surface

An experimental temperature measurement was obtained imaging the interface from above with an infrared camera Gobi-384. This eliminates both the immersion depth effect and the aluminium flakes distortions of the flow. On the other hand, thermography measurements at the fluid interface are not easy[30], since the expected temperature increase are quite small (2 K and 8 K for 40 mW and 300 mW laser power respectively). Such a technique has been successfully used to study the evaporation of sessile water droplets[31]. A thermal image is taken before turning on the laser and another one 30 s after the laser has been turned on. The temperature map shown in Fig. 5a was obtained as the difference between both images. The temperature reading depends on both the camera sensor and ambient temperature and these can change during the measurement. Therefore, sometimes it was necessary to add a constant offset ($< 0.5\,\mathrm{K}$) to the temperature map to make the temperature increase vanish at large distances from the laser spot. Then, the point with the maximum temperature is defined as the laser centre, and the temperature and distance from that centre is computed for each pixel. The results are compared to the simulations as shown in Fig. 5b, fitting C_S to 60. The same experiment was repeated for C_T varying from 1×10^4 to 4×10^4 and the fitting parameter C_S resulted always between 25 and 60. It is worth mentioning that while the convection cell radius strongly depends on C_S, in the conductive regime the maximum temperature does not.

4. Controlled surfactants

Finally, we added a controlled quantity of a known insoluble surfactants to the interface to compare simulations and experiments without any fitting parameter. Oleic acid (OA) was chosen as a surfactant since it has been used in previous works[15]. First, a Langmuir trough (MicroTrough XS, Kibron Inc.) was used to measure the change of surface tension as a function of the surface concentration of OA. The corresponding C_S value as a function of the surface concentration is shown in Fig. 6. Two different regimes are clearly observed. For concentrations below a threshold value ($\Gamma_e = 1.37\,\mathrm{molecule/nm^2}$) the variation of surface pressure with the OA concentration is very low. Meanwhile, for concentrations larger than Γ_e, the surface pressure quickly increases until reaching a saturation.

5 nL and 10 nL and of OA, corresponding to a surface concentration $\Gamma_a = 0.62\,\mathrm{molecule/nm^2}$ and $\Gamma_b = 1.24\,\mathrm{molecule/nm^2}$ ($C_{Sa} = 220$ and $C_{Sb} = 440$) respectively, were added to the inter-
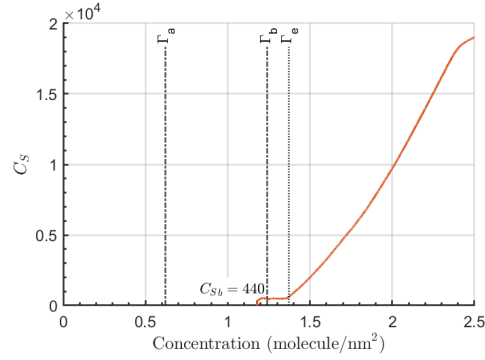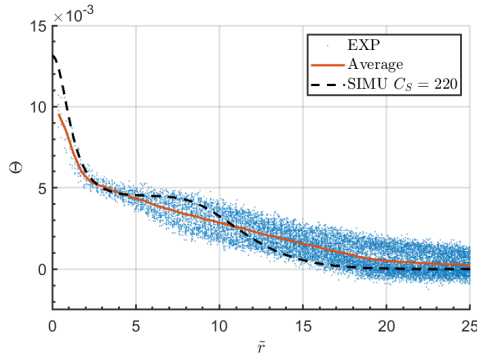
FIG. 6: Characterization of oleic acid (OA) as surfactant. Corresponding C_S value as a function of the surface concentration Γ. Isotherm measurements performed with a Langmuir trough with a compression rate of $2.04\,\text{Å}^2/(\text{min molecule})$. Two regimes are observed with a transition concentration $\Gamma_e = 1.37\,\text{molecule/nm}^2$.

(a) Thermography results with added oleic acid ($\Gamma_a = 0.62\,\text{molecule/nm}^2$ corresponding to $C_S = 220$) and simulations for $C_T = 4 \times 10^4$. We used the same procedure as the one used to obtain Fig. 5b.
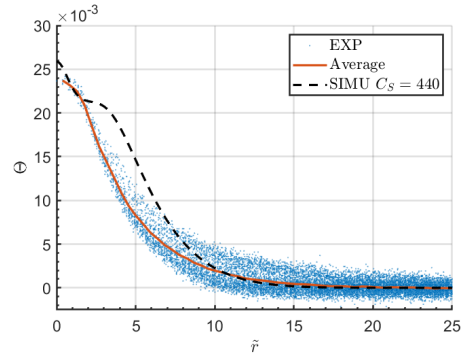
(b) Thermography results with added oleic acid ($\Gamma_b = 1.24\,\text{molecule/nm}^2$ corresponding to $C_S = 440$) and simulations for $C_T = 2 \times 10^4$. We used the same procedure as the one used to obtain Fig. 5b.

FIG. 7: Thermography results with added surfactants.

face. Smaller concentrations produce results that are hard to distinguish from those produced with no added surfactants, and at larger concentrations (above Γ_e), the surface pressure becomes large enough to almost stop the flow. These molecules, besides surface elasticity, could also induce surface shear and dilatational viscosity[32,33]. In our configuration, like in many other experimental setups, the effect of surface elasticity and surface dilatational viscosities cannot be distinguished.

Then, the previously described procedure was followed to perform the thermography measurement. The results agree with the simulation using the corresponding C_S value. When the effect of surfactant is much weaker than the thermocapillary flow, there is a good agreement with simulations as shown in Fig. 7a. On the other hand, when the surfactant concentration becomes higher, there is an agreement with the simulations in the maximum temperature increase as shown in Fig. 7b, but the plateau observed in the simulation is not observed in our experimental measurement. This can be due to second order effects not accounted for in our model, like the induced surface viscosity, or the fact that the added surface surfactant concentration is close to Γ_e where the relationship between surface concentration and surface tension stops being linear, as shown in Fig. 6. Moreover, we cannot guarantee that the initial surfactant concentration was homogeneous over the entire workspace.

We would like to mention that with the added OA, we observe some instabilities at higher laser

powers ($C_T > 4 \times 10^4$). These instabilities can be explained by the competition between the thermocapillary and solutocapillary effects[13,14]. We will not discuss these instabilities here since they are out of the scope of this article.

IV. DISCUSSION

In this section we present an analytical model we have developed to explain our simulations and experimental results. Similar configurations have been analytically analysed[34] under the assumption of negligible momentum and thermal convection could be neglected ($Re << 1$ and $Pe_T << 1$), decoupling the temperature and momentum equations. In such a case, both the fluid velocity and the temperature increase turn out to be proportional to the laser power. However, for the case of water and a convection dominated scenario like ours (local Péclet number $Pe = Pr\,\tilde{u} \approx 100$), no analytical model has been reported. Therefore, we developed a simple model using the concept of boundary layers as it was done in Ref. 35 for the solutocapillary effect. First we analyse the clean interface case (without surfactant). We assume that away from the laser beam ($\tilde{r} > 1$) there are both a viscous and a thermal boundary layers whose thicknesses are[36] respectively

$$\tilde{\delta}_\mu \propto \sqrt{\frac{\tilde{r}}{\tilde{u}_S}} \tag{10a}$$

$$\tilde{\delta}_T = \frac{\tilde{\delta}_\mu}{Pr^{1/2}} \propto \sqrt{\frac{\tilde{r}}{Pr\,\tilde{u}_S}} \tag{10b}$$

where $\tilde{u}_S$ is the non-dimensional radial fluid velocity and the sub-index S means at the interface. If we apply (7) to the interface for $\tilde{r} > 1$ ($\dot{\tilde{q}}_L \approx 0$) under a steady state condition and neglecting the conduction term in the radial direction, we obtain $\tilde{u}_S\,\partial\Theta/\partial\tilde{r} = Pr^{-1}\partial^2\Theta/\partial\tilde{z}^2$. If we approximate at the interface $\partial^2\Theta/\partial\tilde{z}^2 \propto -\Theta_S/\tilde{\delta}_T^2$, the result is

$$\frac{\partial\Theta}{\partial\tilde{r}} \propto -\frac{\Theta_S}{\tilde{r}}. \tag{11}$$

From a surface stress balance point of view, we can approximate at the interface $\partial\tilde{u}/\partial\tilde{z} \propto \tilde{u}_S/\tilde{\delta}_\mu$ and use (11) in (9) obtaining

$$\Theta_S \propto \frac{\tilde{r}^{1/2}\tilde{u}_S^{3/2}}{C_T}. \tag{12}$$

Then, since most of the energy brought by the laser will be evacuated through the thermal boundary layer by convection, i.e. $P_L \propto r\,\delta_{av}\,\rho\,c_p\,(T_S - T_0)\,u_S$, where $\delta_{av} = Pr^{-1/4}\delta_\mu$ is the geometric mean between δ_μ and δ_T. In non-dimensional form, this balance results

$$1 \propto \tilde{r}\,Pr^{3/4}\,\tilde{\delta}_\mu\,\Theta_S\,\tilde{u}_S. \tag{13}$$

Finally, combining (12) and (13) for $\tilde{r} = 1$, and assuming $\tilde{u}_{max} \approx \tilde{u}_S(\tilde{r} = 1)$ and $\Theta_{max} \approx \Theta_S(\tilde{r} = 1)$ we obtain

$$\tilde{u}_{max} = A\,C_T^{1/2}\,Pr^{-3/8} \tag{14}$$

$$\Theta_{max} = B\,C_T^{-1/4}\,Pr^{-9/16}. \tag{15}$$

We can fit the simulations results with $A = 0.43$ and $B = 0.54$ as shown in Figs. 8a and 8b respectively. Experimental temperature results also agree with both simulations and model results. As a comparison, in the case of a conduction dominated scenario[34], it was found that $\tilde{u}_{max} \propto C_T$.

If now we consider the presence of surfactants, we assume that in the convective regime ($1 << \tilde{R}_{cell}$), (14) and (15) are still valid. Under this assumption, we find R_{cell} as the point at which the

thermocapillary and solutocapillary effect cancel each other ($C_T \Theta_S \approx C_S$). Therefore, we propose $\tilde{R}_{\text{cell}} = f(C_T \Theta_{\text{max}}/C_S)$, if we assume a power law, we obtain

$$\tilde{R}_{\text{cell}} = E \left(C_T^{3/4} C_S^{-1} Pr^{-9/16} \right)^{\xi}. \tag{16}$$

The simulation results can be fairly fitted with $E = 1.3$ and $\xi = 2/3$ as shown in Fig. 8c. The discrepancy between the model and simulations for $\tilde{R}_{\text{cell}} > 20$ can be explained by the fact that we simulated a finite volume of water ($\tilde{R}_r \approx 40$).

We simulated all the combinations of $Pr = 1$, 3, 7 and 14, $C_T = (5, 10, 20$ and $40) \times 10^3$; and $C_S = 10$, 20, 40 and 80. When $\tilde{R}_{\text{cell}} \approx 1$ (approaching the transition regime), the velocity $\tilde{u}_{\text{max}}$ becomes smaller than the value predicted by the model and Θ_{max} becomes larger than the value predicted by the model.

V. CONCLUSION

In this manuscript, we analysed the effect of an adsorbed layer of surfactants on a laser-induced thermocapillary flow. Qualitatively, an infrared laser is pointed towards a water volume from above, locally heating the air-water interface. The temperature gradient triggers an interfacial thermocapillary flow away from the laser spot. Due to the mass conservation, a flow towards the laser spot arises deep below the surface, generating a toroidal-like convection cell around the laser spot. The interfacial flow generates a depletion of surfactants around the laser spot, increasing the surface tension and counteracting the effect of the temperature. Analysing the problem, we found 4 governing non-dimensional parameters (besides geometric ones): $Pr = \mu c_p / \kappa$ is the Prandtl number, $Sc = \mu / \rho D_S$ is the surface Schmidt number, $C_T = \rho \gamma_T P_L / \mu^2 \kappa$ is the thermocapillary number (non-dimensional laser power), and $C_S = \rho \gamma_\Gamma \Gamma_0 R_L / \mu^2$ is the solutocapilary number (non-dimensional surfactant concentration).

A numerical thermo-soluto capillary model was developed and applied to the problem described above. This model suggests that a (no matter how small) surfactant concentration affects the thermocapillary flow, reducing the size of the convection cell. Its results were compared with three different experimental observations (PTV, convection cell radius and thermography). The PTV and convection cell radius measurements are more sensitive to the surface contamination, but they necessarily modify the flow by introducing particles in it. On the other hand, the thermography measurement allowed us to obtain the temperature distribution at the interface, but this measurement is less sensitive to the surface contamination than the convection cell radius. Firstly, we performed these measurements on different water samples with an uncontrolled surface contamination, obtaining good agreement with the same range for C_S between 25 and 75. Then, a known quantity of oleic acid was added as surfactant and the thermography measurements was repeated. The result was in good agreement with the simulations using the corresponding value for $C_S = 220$ and $C_S = 440$, thus validating the numerical model without fitting parameters.

Also, a simplified analytical model was developed for sufficiently low values of C_S. We observed a good agreement between this model and the numerical one in the explored range of parameters (Pr, C_T and C_S). We are confident that this simple model can be extended to other configurations as long as thermal convection dominates over conduction.

Such a system could be used to determine the level of contamination of an air-water interface. The convection cell radius measurement is very sensitive to the initial surface contamination level and could be used to characterize slightly contaminated interfaces where a simple surface tension measurement would not have enough resolution. On the other hand, the study of the flow gives us insights towards the miniaturization of the manipulation platform[17] giving the parameters defining the range of the thermocapillary flow. For example, we see that by increasing slightly the surface concentration of surfactants, we could reduce the range of the thermocapillary flow without reducing its effect close to the laser spot.

SUPPLEMENTARY MATERIAL

See supplementary material for the expanded governing equations in cylindrical coordinates, details on the geometry discretization, a discussion on the chosen threshold value to define the simulations cell radius, and an analysis of the effect of each governing non-dimensional parameter in the surface velocity and temperature.

ACKNOWLEDGMENTS

DATA AVAILABILITY STATEMENT

The data that support the findings of this study are available from the corresponding author upon reasonable request.

[1] L. E. Scriven and C. V. Sternling, "The Marangoni effects," Nature **187**, 186–188 (1960).

[2] K. Mills, B. Keene, R. Brooks, and A. Shirali, "Marangoni effects in welding," Philosophical Transactions of the Royal Society of London. Series A: Mathematical, Physical and Engineering Sciences **356**, 911–925 (1998).

[3] F. Preisser, D. Schwabe, A. Scharmann, *et al.*, "Steady and oscillatory thermocapillary convection in liquid columns with free cylindrical surface," Journal of Fluid Mechanics **126**, 545–567 (1983).

[4] G. J. Amador, A. F. Tabak, Z. Ren, Y. Alapan, O. Yasa, and M. Sitti, "Thermocapillary-driven fluid flow within microchannels," arXiv preprint arXiv:1802.00475 (2018).

[5] Y. Zhao, D. Wan, X. Chen, X. Chao, and H. Xu, "Uniform breaking of liquid-jets by modulated laser heating," Physics of Fluids **33**, 044115 (2021).

[6] Y. S. Ryazantsev, M. G. Velarde, R. G. Rubio, E. Guzmán, F. Ortega, and P. López, "Thermo-and soluto-capillarity: Passive and active drops," Advances in colloid and interface science **247**, 52–80 (2017).

[7] K.-X. Hu, C.-Y. Yan, and Q.-S. Chen, "Instability of thermocapillary–buoyancy convection in droplet migration," Physics of Fluids **31**, 122101 (2019).

[8] M. A. Rahman, J. Cheng, Z. Wang, and A. T. Ohta, "Cooperative micromanipulation using the independent actuation of fifty microrobots in parallel," Scientific reports **7**, 1–11 (2017).

[9] M. Lu, J. Lu, Y. Zhang, and G. Tryggvason, "Numerical study of thermocapillary migration of a bubble in a channel with an obstruction," Physics of Fluids **31**, 062101 (2019).

[10] K. Dietrich, N. Jaensson, I. Buttinoni, G. Volpe, and L. Isa, "Microscale Marangoni surfers," Physical Review Letters **125**, 098001 (2020).

[11] E. Lucassen-Reynders, A. Cagna, and J. Lucassen, "Gibbs elasticity, surface dilational modulus and diffusional relaxation in nonionic surfactant monolayers," Colloids and Surfaces A: Physicochemical and Engineering Aspects **186**, 63–72 (2001).

[12] L. Champougny, B. Scheid, F. Restagno, J. Vermant, and E. Rio, "Surfactant-induced rigidity of interfaces: a unified approach to free and dip-coated films," Soft Matter **11**, 2758–2770 (2015).

[13] A. Mizev, A. Shmyrov, and A. Shmyrova, "On the shear-driven surfactant layer instability," arXiv preprint arXiv:2101.02485 (2021).

[14] G. Koleski, A. Vilquin, J.-C. Loudet, T. Bickel, and B. Pouligny, "Azimuthal instability of the radial thermocapillary flow around a hot bead trapped at the water–air interface," Physics of Fluids **32**, 092108 (2020).

[15] A. Shmyrov, A. Mizev, V. Demin, M. Petukhov, and D. Bratsun, "On the extent of surface stagnation produced jointly by insoluble surfactant and thermocapillary flow," Advances in Colloid and Interface Science **255**, 10 – 17 (2018), multiscale Applications of Surface Tension and Capillary Forces.

[16] R. Terrazas M., A. Bolopion, J. Beugnot, P. Lambert, and M. Gauthier, "Laser-induced thermocapillary convective flows: A new approach for noncontact actuation at microscale at the fluid/gas interface," IEEE/ASME Transactions on Mechatronics **22**, 693–704 (2017).

[17] F. N. Piñan Basualdo, A. Bolopion, M. Gauthier, and P. Lambert, "A microrobotic platform actuated by thermocapillary flows for manipulation at the air-water interface," Science Robotics **6** (2021), 10.1126/scirobotics.abd3557, https://robotics.sciencemag.org/content/6/52/eabd3557.full.pdf.

[18] T. B. Nguyen and C. M. Phan, "Influence of hydrophilicity on the thermal-driven surfactant flow at the air/water surface," ACS omega **3**, 9060–9065 (2018).

[19] J. Eastoe and J. Dalton, "Dynamic surface tension and adsorption mechanisms of surfactants at the air–water interface," Advances in Colloid and Interface Science **85**, 103 – 144 (2000).

[20]H. A. Stone, "A simple derivation of the time-dependent convective-diffusion equation for surfactant transport along a deforming interface," Physics of Fluids A: Fluid Dynamics **2**, 111–112 (1990), https://doi.org/10.1063/1.857686.

[21]A. K. Sen and S. H. Davis, "Steady thermocapillary flows in two-dimensional slots," Journal of Fluid Mechanics **121**, 163–186 (1982).

[22]B. Messmer, T. Lemee, K. Ikebukuro, I. Ueno, and R. Narayanan, "Confined thermo-capillary flows in a double free-surface film with small Marangoni numbers," International Journal of Heat and Mass Transfer **78**, 1060–1067 (2014).

[23]H. Chraïbi and J.-P. Delville, "Thermocapillary flows and interface deformations produced by localized laser heating in confined environment," Physics of Fluids **24**, 032102 (2012).

[24]P. Kosky, R. Balmer, W. Keat, and G. Wise, "Chapter 14 - mechanical engineering," in *Exploring Engineering (Fifth Edition)*, edited by P. Kosky, R. Balmer, W. Keat, and G. Wise (Academic Press, 2021) fifth edition ed., pp. 317–340.

[25]T. Dracos, "Particle tracking velocimetry (ptv)," in *Three-Dimensional Velocity and Vorticity Measuring and Image Analysis Techniques* (Springer, 1996) pp. 155–160.

[26]S. Ferrari and L. Rossi, "Particle tracking velocimetry and accelerometry (ptva) measurements applied to quasi-two-dimensional multi-scale flows," Experiments in fluids **44**, 873–886 (2008).

[27]A. Prasad, "Particle image velocimetry," Current science **79**, 51–60 (2000).

[28]S. Dehaeck, P. Queekers, and P. Colinet, "Analyse par ptv du champ de vitesse de surface dans l'instabilité de Marangoni-Bénard," in *Congrès Francophone de Techniques Laser* (2010).

[29]D. Vella, "Floating versus sinking," Annual Review of Fluid Mechanics **47**, 115–135 (2015).

[30]R. G. Rubio, Y. S. Ryazantsev, V. M. Starov, G.-X. Huang, A. P. Chetverikov, P. Arena, A. A. Nepomnyashchy, A. Ferrus, and E. G. Morozov, "Without bounds: A scientific canvas of nonlinearity and complex dynamics," (Springer, 2013) Chap. Thermography Applied to Interfacial Phenomena, Potentials and Pitfalls, pp. 157–182.

[31]F. Girard, M. Antoni, and K. Sefiane, "Infrared thermography investigation of an evaporating sessile water droplet on heated substrates," Langmuir **26**, 4576–4580 (2010), pMID: 20199075, https://doi.org/10.1021/la9048659.

[32]J. Earnshaw, "Surface viscosity of water," Nature **292**, 138–139 (1981).

[33]A. Choudhury, V. K. Paidi, S. K. Kalpathy, and H. N. Dixit, "Enhanced stability of free viscous films due to surface viscosity," Physics of Fluids **32**, 082108 (2020).

[34]T. Bickel, "Effect of surface-active contaminants on radial thermocapillary flows," The European Physical Journal E **42**, 1–9 (2019).

[35]M. Roché, Z. Li, I. M. Griffiths, S. Le Roux, I. Cantat, A. Saint-Jalmes, and H. A. Stone, "Marangoni flow of soluble amphiphiles," Phys. Rev. Lett. **112**, 208302 (2014).

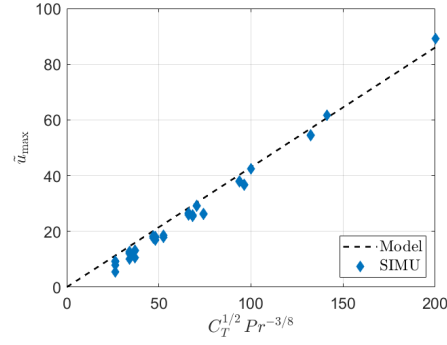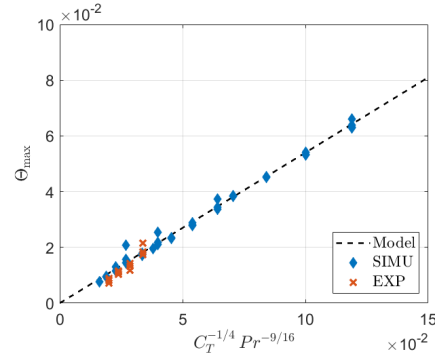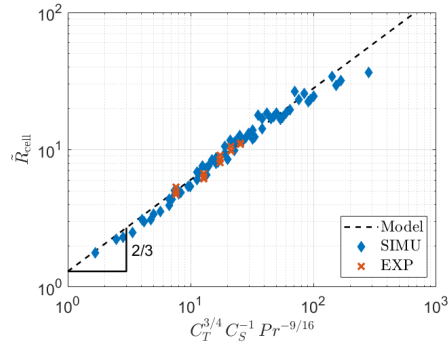[36]H. Schlichting and K. Gersten, *Boundary-layer theory* (Springer, 2016).

(a) Maximum surface fluid velocity $\tilde{u}_S$.

(b) Maximum surface temperature Θ_S.

(c) Convection cell radius $\tilde{R}_{\text{cell}}$.

FIG. 8: Comparison between the simplified model (14), (15) and (16), the simulation results and experimental measurements. For the simulations results, we simulated all the combinations of $Pr = 1$, 3, 7 and 14; $C_T = (5, 10, 20 \text{ and } 40) \times 10^3$; and $C_S = 10$, 20, 40 and 80.

SUPPLEMENTARY MATERIAL

A. Equations in cylindrical coordinates

The mass, radial and vertical momentum, and energy equations in cylindrical coordinates result:

$$\frac{1}{r}\frac{\partial(ru)}{\partial r} + \frac{\partial v}{\partial z} = 0 \tag{S1}$$

$$\rho\left(\frac{\partial u}{\partial t} + u\frac{\partial u}{\partial r} + v\frac{\partial u}{\partial z}\right) = -\frac{\partial P}{\partial r} + \mu\left(\frac{1}{r}\frac{\partial}{\partial r}\left(r\frac{\partial u}{\partial r}\right) - \frac{u}{r^2} + \frac{\partial^2 u}{\partial z^2}\right) \tag{S2}$$

$$\rho\left(\frac{\partial v}{\partial t} + u\frac{\partial v}{\partial r} + v\frac{\partial v}{\partial z}\right) = -\frac{\partial P}{\partial z} + \mu\left(\frac{1}{r}\frac{\partial}{\partial r}\left(r\frac{\partial v}{\partial r}\right) + \frac{\partial^2 v}{\partial z^2}\right) \tag{S3}$$

$$\rho c_p\left(\frac{\partial T}{\partial t} + u\frac{\partial T}{\partial r} + v\frac{\partial T}{\partial z}\right) = \kappa\left(\frac{1}{r}\frac{\partial}{\partial r}\left(r\frac{\partial T}{\partial r}\right) + \frac{\partial^2 T}{\partial z^2}\right) + \dot{q}_L \tag{S4}$$

where the cylindrical symmetry was assumed, u and v are the radial and vertical components of the velocity. The surface surfactant transport (3) and the surface stress balance (2) in cylindrical coordinates and assuming a flat interface result

$$\frac{\partial\Gamma}{\partial t} + \frac{1}{r}\frac{\partial(ru\Gamma)}{\partial r} = D_S\frac{1}{r}\frac{\partial}{\partial r}\left(r\frac{\partial\Gamma}{\partial r}\right) \tag{S5}$$

$$\mu\frac{\partial u}{\partial z} = -\left(\gamma_T\frac{\partial T}{\partial r} + \gamma_\Gamma\frac{\partial\Gamma}{\partial r}\right) \tag{S6}$$

The non-dimensional version of (S1), (S2), (S3) and (S4) result

$$\frac{1}{\tilde{r}}\frac{\partial(\tilde{r}\tilde{u})}{\partial\tilde{r}} + \frac{\partial\tilde{v}}{\partial\tilde{z}} = 0 \tag{S7}$$

$$\frac{\partial\tilde{u}}{\partial\tilde{t}} + \tilde{u}\frac{\partial\tilde{u}}{\partial\tilde{r}} + \tilde{v}\frac{\partial\tilde{u}}{\partial\tilde{z}} = -\frac{\partial\tilde{P}}{\partial\tilde{r}} + \frac{1}{\tilde{r}}\frac{\partial}{\partial\tilde{r}}\left(\tilde{r}\frac{\partial\tilde{u}}{\partial\tilde{r}}\right) - \frac{\tilde{u}}{\tilde{r}^2} + \frac{\partial^2\tilde{u}}{\partial\tilde{z}^2} \tag{S8}$$

$$\frac{\partial\tilde{v}}{\partial\tilde{t}} + \tilde{u}\frac{\partial\tilde{v}}{\partial\tilde{r}} + \tilde{v}\frac{\partial\tilde{v}}{\partial\tilde{z}} = -\frac{\partial\tilde{P}}{\partial\tilde{z}} + \frac{1}{\tilde{r}}\frac{\partial}{\partial\tilde{r}}\left(\tilde{r}\frac{\partial\tilde{v}}{\partial\tilde{r}}\right) + \frac{\partial^2\tilde{v}}{\partial\tilde{z}^2} \tag{S9}$$

$$\frac{\partial\Theta}{\partial\tilde{t}} + \tilde{u}\frac{\partial\Theta}{\partial\tilde{r}} + \tilde{v}\frac{\partial\Theta}{\partial\tilde{z}} = \frac{1}{Pr}\left(\frac{1}{\tilde{r}}\frac{\partial}{\partial\tilde{r}}\left(\tilde{r}\frac{\partial\Theta}{\partial\tilde{r}}\right) + \frac{\partial^2\Theta}{\partial\tilde{z}^2} + \dot{\tilde{q}}_L\right) \tag{S10}$$

where $\dot{\tilde{q}}_L = 2\psi\exp\left(-2\tilde{r}^2 + \psi\tilde{z}\right)/\pi$ is the dimensionless absorbed volumetric power, $\psi = \alpha R_L$ describes the aspect ratio of the heated volume, $Pr = \mu c_p/\kappa$ is the Prandtl number. At the interface, the non-dimensional version of (S5), (S6) result

$$\frac{\partial\tilde{\Gamma}}{\partial\tilde{t}} + \frac{1}{\tilde{r}}\frac{\partial(\tilde{r}\tilde{u}\tilde{\Gamma})}{\partial\tilde{r}} = \frac{1}{Sc}\frac{1}{\tilde{r}}\frac{\partial}{\partial\tilde{r}}\left(\tilde{r}\frac{\partial\tilde{\Gamma}}{\partial\tilde{r}}\right) \tag{S11}$$

$$\frac{\partial\tilde{u}}{\partial\tilde{z}} = -\left(C_T\frac{\partial\Theta}{\partial\tilde{r}} + C_S\frac{\partial\tilde{\Gamma}}{\partial\tilde{r}}\right) \tag{S12}$$

where $Sc = \mu/\rho D_S$ is the surface Schmidt number, $C_T = \rho\gamma_T P_L/\mu^2\kappa$ is the thermocapillary number, and $C_S = \rho\gamma_\Gamma\Gamma_0 R_L/\mu^2$ is the solutocapillary number.

B. Simulations: geometry discretization and cell radius definition

Finite elements, axisymmetric, time dependent simulations were performed using Comsol multiphysics with the parameters shown in Table II, $\tilde{H}_r = 10$, and $\tilde{R}_r = 40$. We used a quadrilateral mesh to discretize the geometry, with finer elements close to the interface and close to the laser spot (symmetry axis). The minimum non-dimensional element size was 0.09 and the maximum is 0.44.
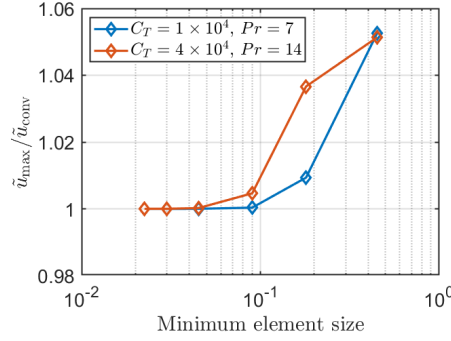
FIG. S1: Maximum non-dimensional velocity $\tilde{u}$ (normalized by the converged value) as a function of the non-dimensional minimum element size for $\tilde{t} = 25$, $C_S = 40$, $Sc = 10$, $\psi = 2$. Two curves are shown, the standard case ($C_T = 1 \times 10^4$ and $Pr = 7$), and the worst-case scenario ($C_T = 4 \times 10^4$ and $Pr = 14$).
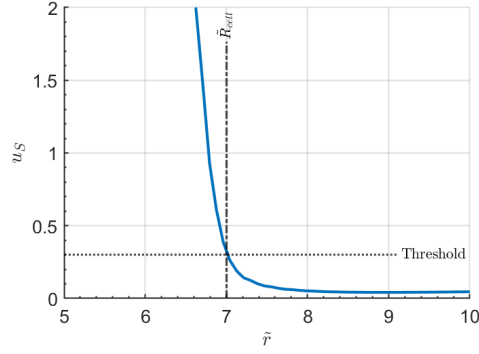

FIG. S2: Surface non-dimensional velocity $\tilde{u}_S$ as a function of the non-dimensional radius $\tilde{r}$ for $\tilde{t} = 25$, $C_T = 1 \times 10^4$, $C_S = 40$, $Pr = 7$, $Sc = 10$, $\psi = 2$. We observe that the obtained value of $\tilde{R}_{\text{cell}}$ is not sensitive to the threshold value in the range 0.3 to 1.0.

The convergence of the simulations was verified for the standard case and the worst-case as shown in Fig. S1. For the worst case scenario, the simulation seems not to be completely converged, but the variation with respect to the converged value is less than 0.5 %. We used a P2+P1 discretization for the momentum, and a quadratic Lagrange for the energy and surfactant transport equations.

On the other hand, we need to define a threshold velocity value to define the size of the cell, since the surface velocity never reaches zero due, presumably, to numerical errors. The results are almost not sensitive to the threshold value in the range 0.3 to 1.0 as shown in Fig. S2. Therefore, we decided to take the lowest value in this range (0.3) as the threshold value for all simulation results.

C. Surface velocity and temperature dependence on the governing non-dimensional numbers

The effect of Pr and C_T on the surface variables is shown in Figs. S3 and S4 respectively. It can be seen how decreasing the Prandtl number (Pr) has a similar effect than increasing the thermocapillary number (C_T).

The effect of C_S on the surface variables is shown in Fig. S5. For $C_S < 40$, the convection cell radius strongly depends on C_S, but the maximum velocity remains almost constant. For $C_S > 40$, the maximum fluid velocity starts to diminish as $\tilde{R}_{\text{cell}}$ approaches unity. On the other hand, we observe how the temperature distribution remains almost constant for $C_S < 40$. For $C_S > 40$, the maximum temperature starts to increase due to the reduced convection.
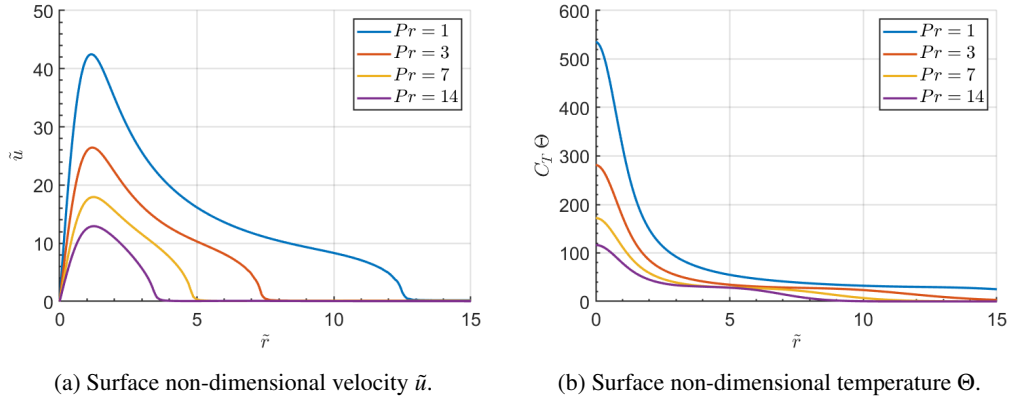
(a) Surface non-dimensional velocity $\tilde{u}$.

(b) Surface non-dimensional temperature Θ.

FIG. S3: Surface simulation results for $\tilde{t} = 25$, $C_T = 1 \times 10^4$, $C_S = 40$, $Sc = 10$, $\psi = 2$, and different values of Pr.
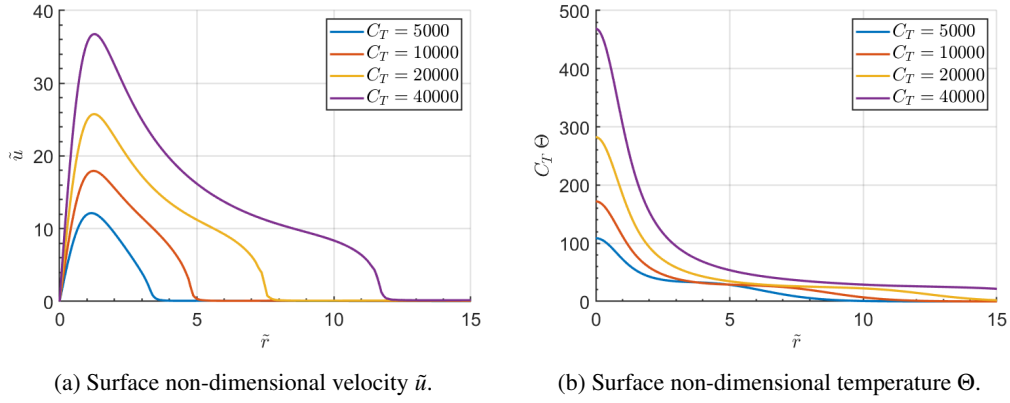

(a) Surface non-dimensional velocity $\tilde{u}$.

(b) Surface non-dimensional temperature Θ.

FIG. S4: Surface simulation results for $\tilde{t} = 25$, $C_S = 40$, $Pr = 7$, $Sc = 10$, $\psi = 2$, and different values of C_T.

(a) Surface non-dimensional velocity $\tilde{u}$.

(b) Surface non-dimensional temperature Θ.
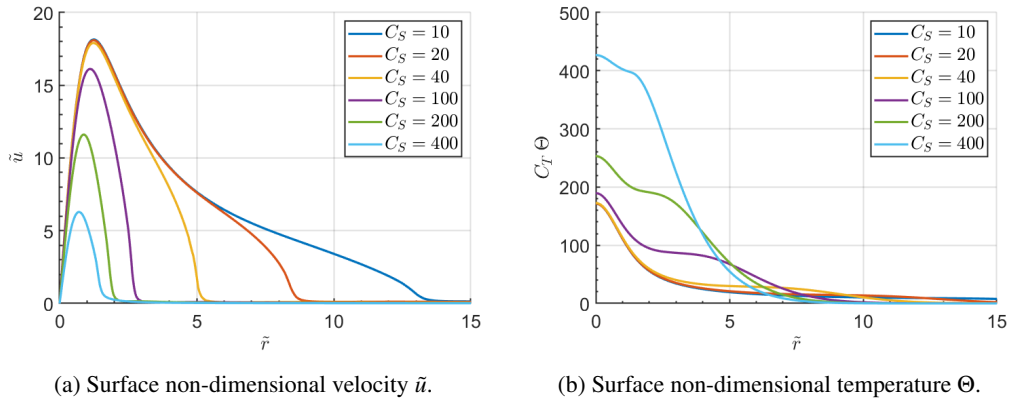
FIG. S5: Surface simulation results for $\tilde{t} = 25$, $C_T = 1 \times 10^4$, $Pr = 7$, $Sc = 10$, $\psi = 2$, and different values of C_S.
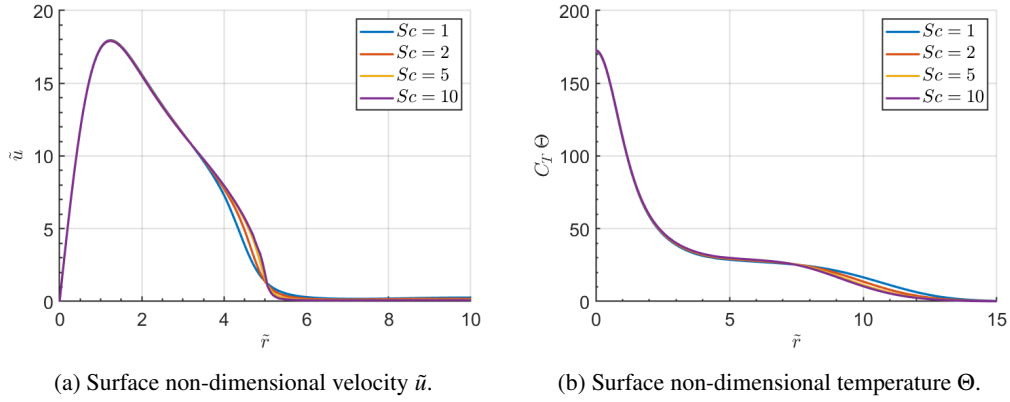
(a) Surface non-dimensional velocity $\tilde{u}$.

(b) Surface non-dimensional temperature Θ.

FIG. S6: Surface simulation results for $\tilde{t} = 25$, $C_T = 1 \times 10^4$, $C_S = 40$, $Pr = 7$, $\psi = 2$, and different values of Sc.

(a) Surface non-dimensional velocity $\tilde{u}$.

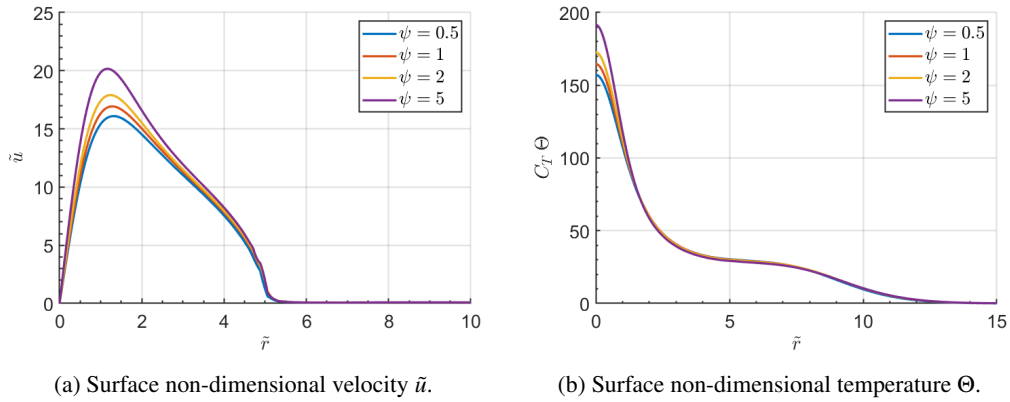(b) Surface non-dimensional temperature Θ.

FIG. S7: Surface simulation results for $\tilde{t} = 25$, $C_T = 1 \times 10^4$, $C_S = 40$, $Pr = 7$, $Sc = 10$ and different values of ψ.

The effect of Sc and ψ on the surface variables is shown in Figs. S6 and S7 respectively. It can be seen that both the surface velocity and temperature distribution do not strongly depend on the Sc and ψ values. The fact that Sc does not have an strong impact on the system can be explained by the fact that the surfactant transport is dominated by convection and not diffusion.